

Electronic Supplementary Information

Monolithically integrated, photo-rechargeable portable power sources based on miniaturized Si solar cells and printed solid-state lithium-ion batteries

Han-Don Um[†], Keun-Ho Choi[†], Inchan Hwang, Se-Hee Kim, Kwanyong Seo* and Sang-Young Lee*

Department of Energy Engineering, School of Energy and Chemical Engineering, Ulsan National Institute of Science and Technology (UNIST), Ulsan 44919, Korea

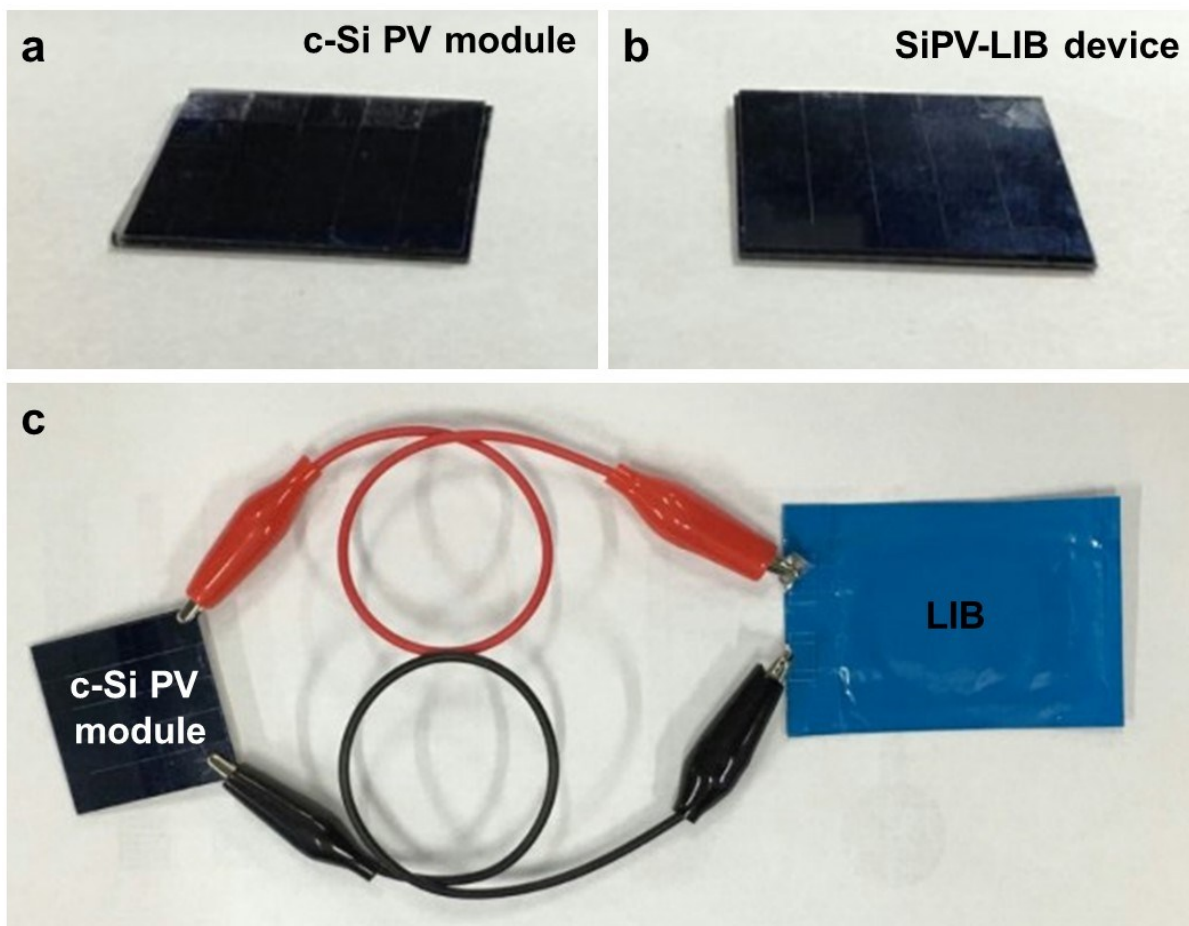
[†]These authors contributed equally to this work.

*email: kseo@unist.ac.kr; syleek@unist.ac.kr

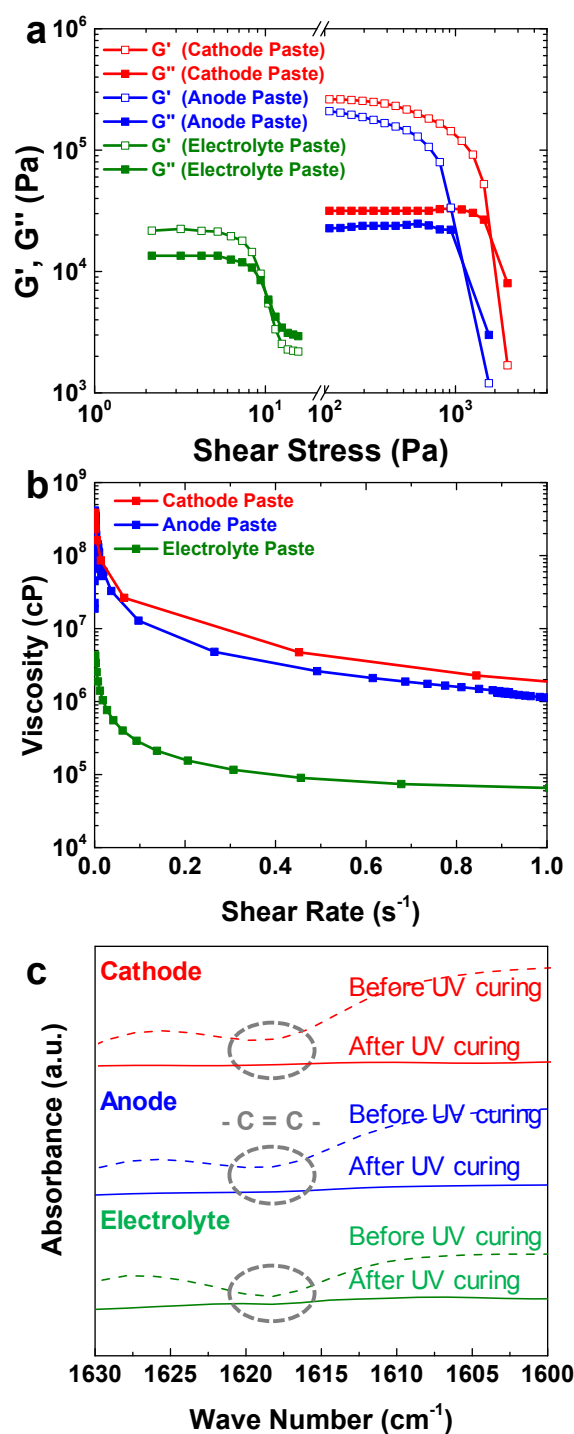
Supplementary Note 1. Fabrication and characteristics of single Si solar cell

The c-Si solar cells were designed with both negative and positive polarity contacts at the rear surface of the solar cells. Supplementary Fig. S5a illustrates the layout of a single c-Si solar cell and highlights the doped regions, such as the emitter (p^+ , red), base (n, blue), and back surface field (n^+ , deep blue). The back of the cell consists of an interdigitated emitter and a back surface field formed by the selective-area diffusion of boron and phosphorus; the doping processes result in the formation of p-n junctions and ohmic contacts. The surface doping concentrations of the emitter (boron) and back surface field (phosphorus) regions are $2.0 \times 10^{19} \text{ cm}^{-3}$ and $2.0 \times 10^{20} \text{ cm}^{-3}$, respectively, as measured by secondary ion mass spectrometry (Supplementary Fig. S5b). The entire surface, except for the emitter and back surface field regions, was coated by aluminium oxide (Al_2O_3) and silicon nitride (SiN_x), which serves not only to minimize the surface recombination but also to prevent the electrical connection between the emitter and back surface field. For metal grids, the grid patterns were formed using photolithography at the emitter and back surface field regions, followed by the thermal deposition of a 500-nm-thick Al film. Current density–voltage (J – V) characteristics of the single c-Si solar cells with a size of 36 mm^2 (length x width = 6×6 (mm x mm)) were measured in the dark environment and under AM 1.5 G illumination (100 W cm^{-2}) at room temperature, as shown in Supplementary Fig. S5c. Based on the analysis of the dark J – V curve (inset of Supplementary Fig. S5c), the diode ideality factor¹ was found to be close to unity ($n = 1.21$), which shows that thermal emission dominated the behaviour of the ideal diode. The J – V curve under illumination shows that the single c-Si cell achieved the highest PCE of 15.7%. The significantly high efficiency of the single c-Si solar cell is primarily attributed to an enhancement of J_{sc} due to the unique design. Because there is no metal electrode on the front surface of the single c-Si solar cell compared to conventional solar cells with a front-back-contact design, the single c-Si solar cell can effectively absorb light without experiencing shading losses (*i.e.*, light reflection from the front metal). Furthermore, the surface recombination velocity of the single c-Si solar cell would be much lower than that of conventional solar cells with deep junction depths and heavy doping in the front surface because the entire front surface with a lightly doped region is fully covered by the passivation layer. The enhancement of J_{sc} in the single c-Si solar cells is consistent with external quantum efficiencies (EQEs) $> 80\%$ in the 500–900 nm wavelength spectrum because the photocarriers generated near the front surface of cells are effectively collected with a low surface recombination velocity (Supplementary Fig. S5d). Supplementary Fig. S5e shows the

statistical analyses of photovoltaic metrics from 25 solar cells fabricated on a single wafer. The low standard deviation for all of the PV metrics indicates the reproducibility and robustness of our device design, which enables the development of compact/portable power generation devices.

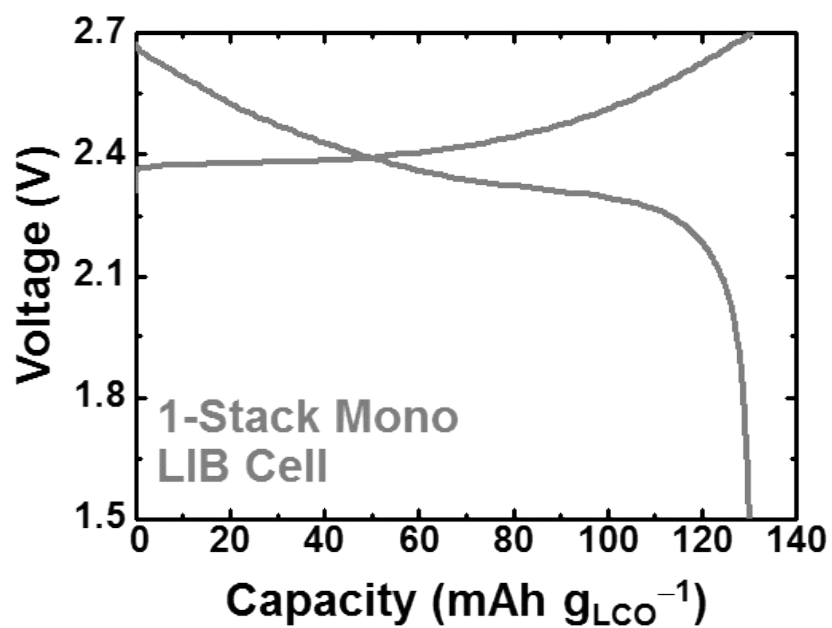


Supplementary Fig. S1. (a) Digital photograph of the c-Si PV module. (b) Digital photograph of the SiPV-LIB device. (c) Digital photograph showing a typical connection between the PV module and LIB via electric wires.

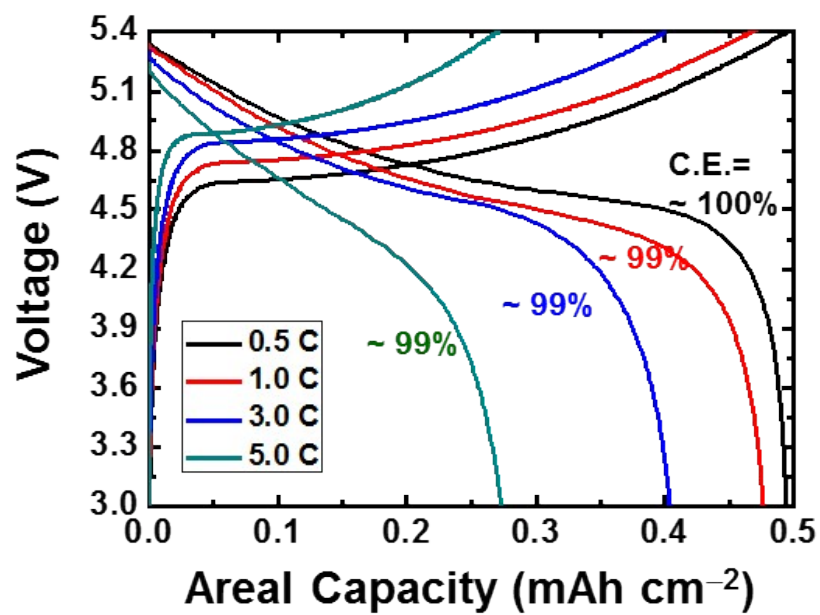


Supplementary Fig. S2. Rheological properties. (a) viscosity and (b) viscoelasticity represented by the storage modulus (G') and loss modulus (G''), of printable cell components prior to UV curing. The cathode paste consists of an active material mixture/electrolyte precursor mixture with a ratio of 60/40 (w/w), wherein the active material mixture is LCO/carbon black (80/20 (w/w)) and the electrolyte precursor mixture is ETPTA/1M $LiPF_6$ in EC/PC (1/1 (v/v) = 15/85 (w/w)). The anode paste consists of an active material

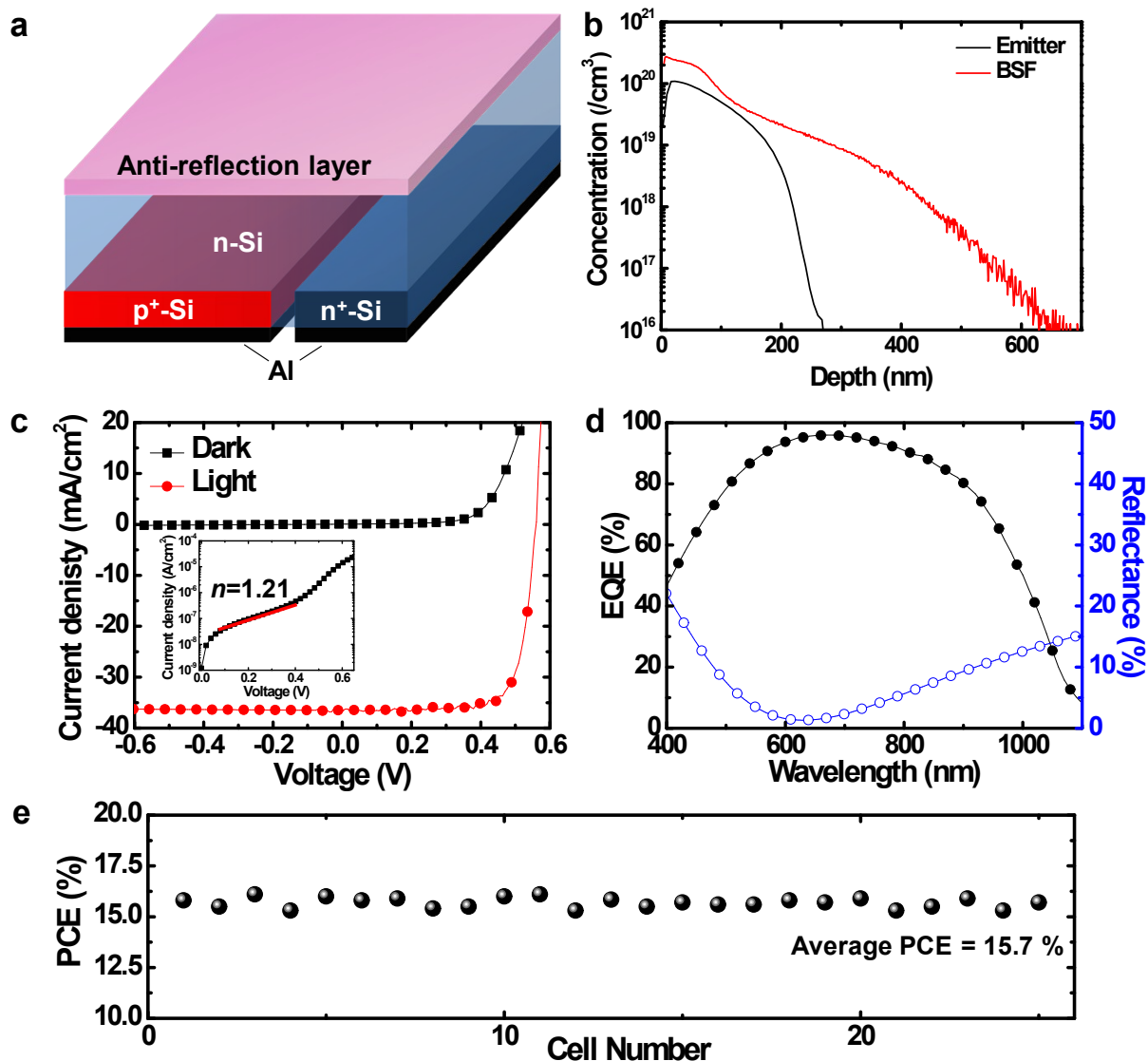
mixture/electrolyte precursor mixture with a ratio of 60/40 (w/w), wherein the active material mixture is LTO/carbon black (80/20 (w/w)) and the electrolyte precursor mixture is the same as the aforementioned one. The solid-state electrolyte paste consists of an Al₂O₃ nanoparticles/electrolyte precursor mixture with a ratio of 50/50 (w/w), where the electrolyte precursor mixture is the same as the aforementioned one. (c) The change in the FT-IR spectra of acrylic C=C double bonds of ETPTA before/after UV curing.



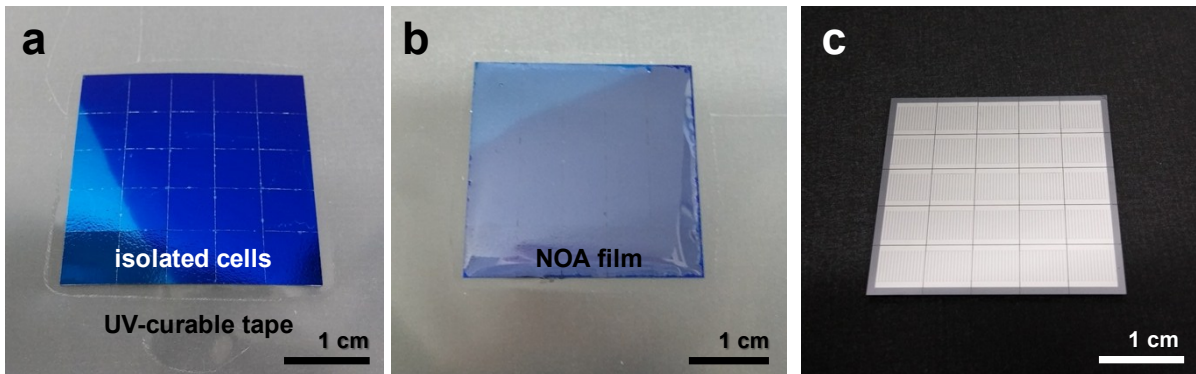
Supplementary Fig. S3. Galvanostatic charge/discharge profiles of the 1-stack mono LIB cell at a charge/discharge current density of 1.0 C/1.0 C.



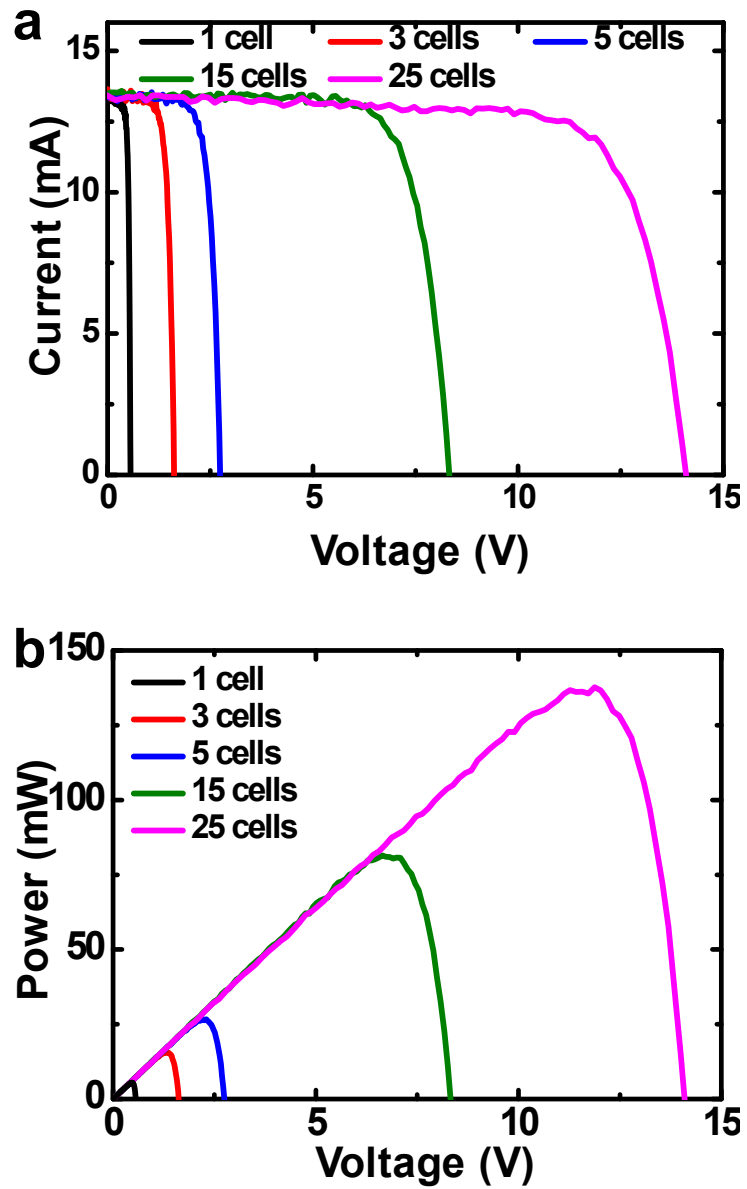
Supplementary Fig. S4. Galvanostatic charge/discharge profiles of bipolar LIB cell in SiPV-LIB device as a function of charge/discharge current densities (varying from 0.5 C/0.5 C to 5.0 C/5.0 C).



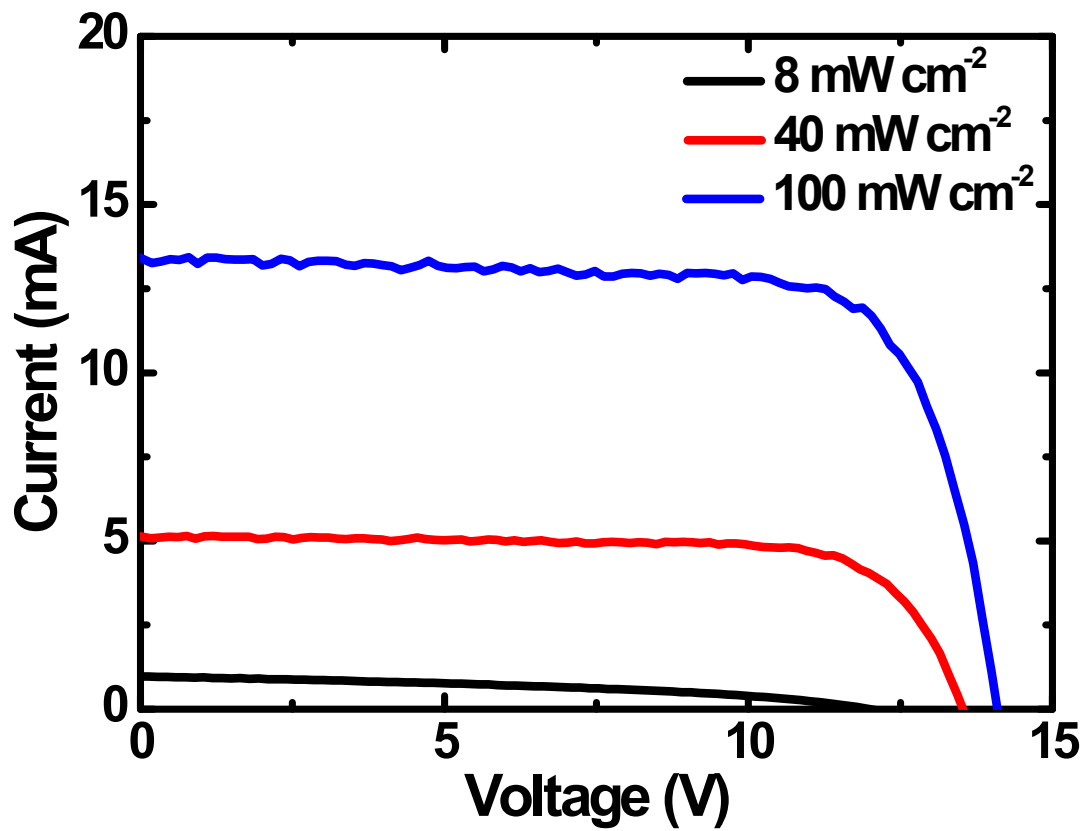
Supplementary Fig. S5. Characterization of single c-Si solar cell. (a) Schematic illustration of a single c-Si solar cell consisting of both negative and positive polarity contacts at the rear surface. (b) Secondary ion mass spectrometry profiles of the emitter (black line) and back surface field (BSF) regions (red line). (c) Current density–voltage (J – V) curves of a single c-Si solar cell in the dark environment (black line with filled squares) and under light illumination (red line with filled circles). Inset shows the same dark J – V curve plotted in a semi-log scale, which indicates the ideality factor (n) of 1.21. (d) External quantum efficiency (EQE, black line with filled circles) and reflectance spectra (blue line with hollow circles) of a single c-Si solar cell. (e) Statistical analysis of the PCE for c-Si solar cells fabricated in the single wafer as a function of cell number.



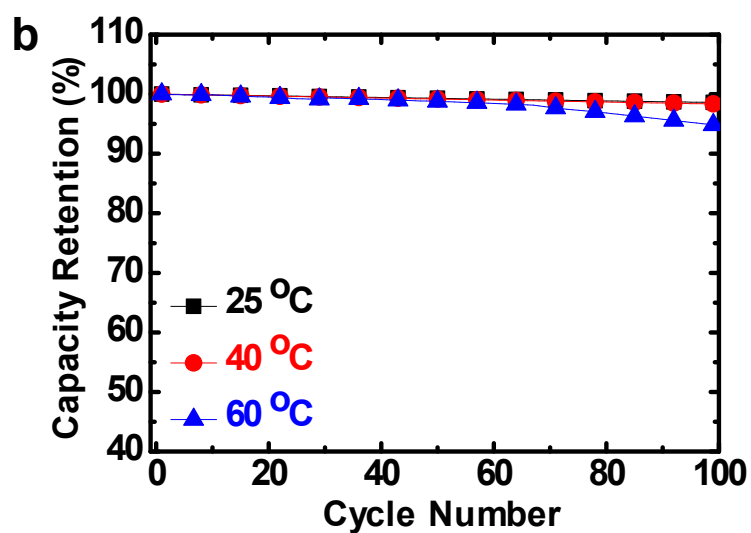
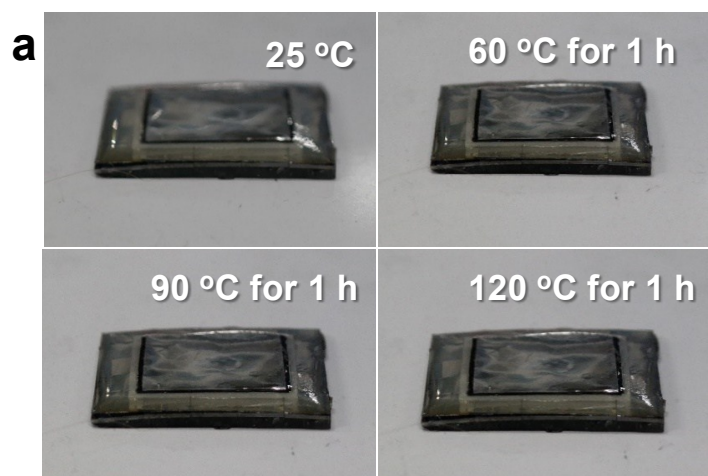
Supplementary Fig. S6. Assembly of compact c-Si PV module. Digital photographs of isolated c-Si solar cells on UV-curable tape (DUV 190, DS Semicon) (a) polymer (NOA 71, Norland Products, Inc.)-embedded c-Si solar cells (b), and tape detachment from the backside of the polymer (NOA 71)-embedded solar cells (c).



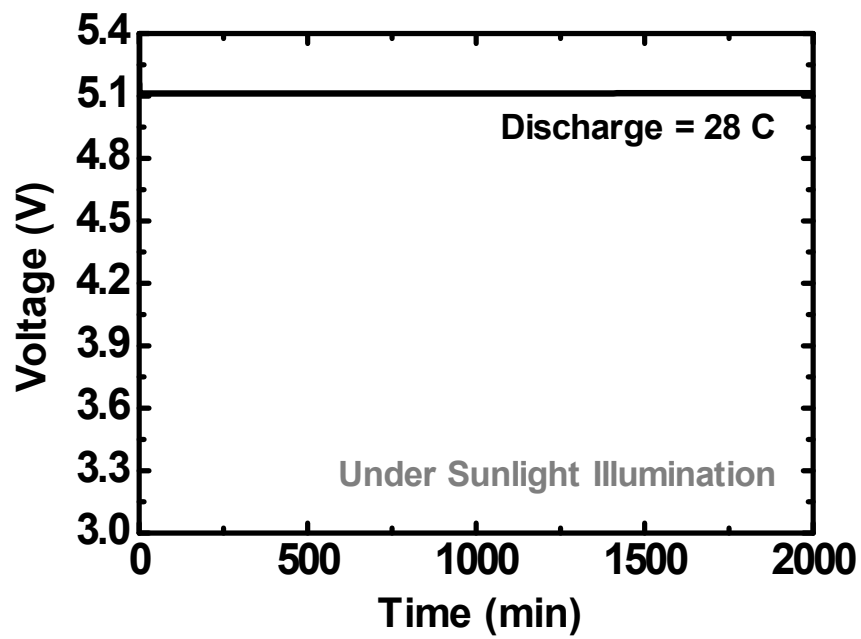
Supplementary Fig. S7. Characterization of c-Si PV module as a function of c-Si mini-cells. (a) Current–voltage curves. (b) Power–voltage curves.



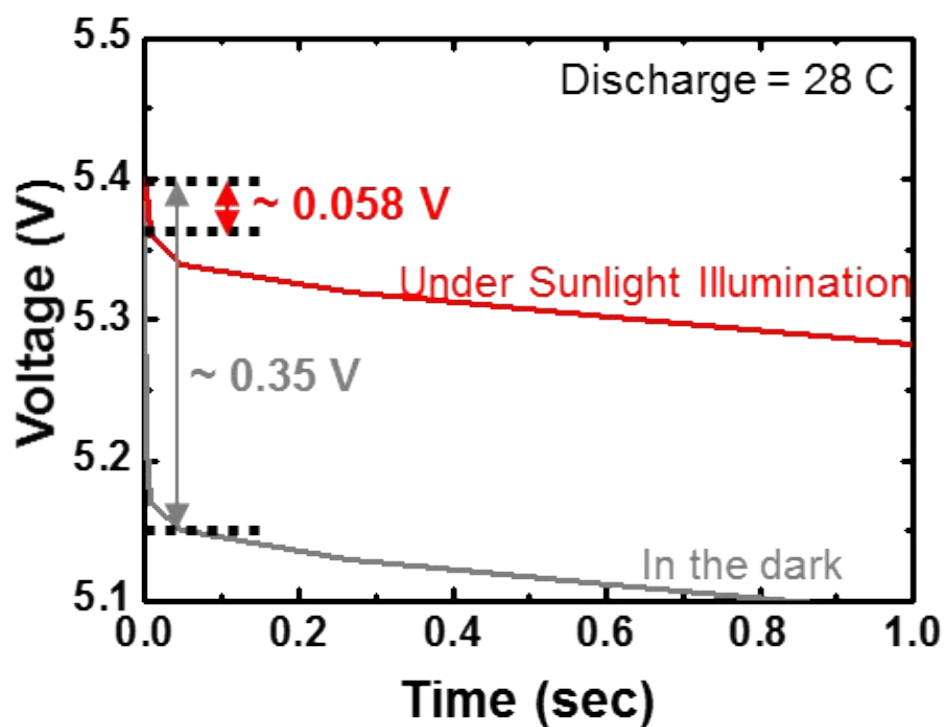
Supplementary Fig. S8. Current-voltage curves that show the photo-induced energy conversion capability of the c-Si PV module in the SiPV-LIB device under various light intensity conditions: 8 (black line), 60 (red line), and 100 (blue line) mW cm⁻².



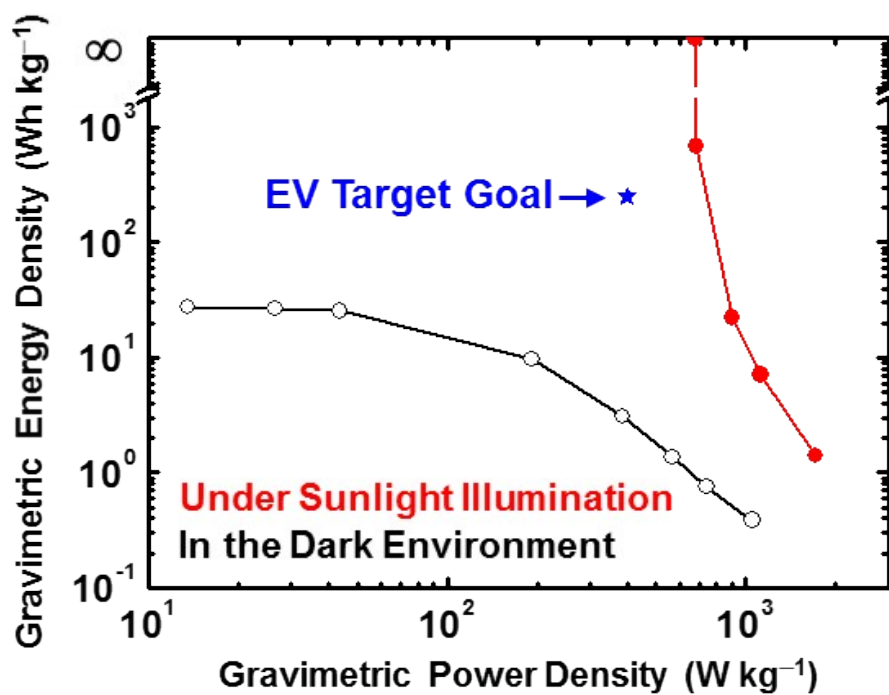
Supplementary Fig. S9. Thermal stability of the SiPV-LIB device. (a) Digital photographs showing the dimensional change of the SiPV-LIB device (with a focus on the LIB part) after it is placed in a hot oven for 1 h with the temperature varied from 60 to 120°C. (b) Capacity retention of SiPV-LIB device with cycling as a function of temperature under a light intensity of 100 mW cm⁻² and a discharge current rate of 1.0 C.



Supplementary Fig. S10. Galvanostatic discharge profile of SiPV-LIB device at a constant discharge current rate (= 28 C) under sunlight illumination at a light intensity of 100 mW cm^{-2} .



Supplementary Fig. S11. Galvanostatic discharge profiles (measured at a discharge current density of 28 C) of the SiPV-LIB device under sunlight illumination (red line) and in the dark environment (grey line). The difference in the initial voltage between the voltage at open-circuit and the voltage at a given discharge current density of 28 C was used to determine the internal resistance ($R_{internal}$) of the LIB.



Supplementary Fig. S12. Ragone plots (gravimetric energy density (Wh kg^{-1}) vs. gravimetric power density (W kg^{-1})) of SiPV-LIB devices under sunlight illumination (red line) and in the dark environment (black line).



Supplementary Movie S1. Video clips showing portable electronics that are being charged by SiPV-LIB device under sunlight illumination. (a) smartphone. (b) MP3 player.

Supplementary Table S1. Photovoltaic parameters of a single c-Si solar cell and the compact c-Si PV module.

Number of interconnected cells	V_{oc} (V)	I_{sc} (mA cm ⁻²)	Cell area (cm ²)	J_{sc} (mA cm ⁻²)	FF (%)	Max power (mW)	PCE (%)
1 cell	0.56±0.01	13.2±0.06	0.36	36.7±0.10	76.5±0.26	5.7±0.13	15.7±0.25
3 cells	1.63±0.15	13.4±0.20	1.08	12.4±0.18	77.2±0.43	16.9±0.39	15.6±0.43
5 cells	2.74±0.20	13.3±0.13	1.8	7.4±0.07	77.0±0.17	28.1±0.55	15.6±0.16
15 cells	8.34±0.15	13.5±0.08	5.4	2.5±0.01	76.7±0.42	86.4±4.62	15.6±0.21
25 cells	14.15±0.10	13.4±0.11	9	1.5±0.01	75.2±0.50	142.6±6.38	15.8±0.62

Supplementary Table S2. Summary of previously reported, single-unit PV-LIB systems.

Energy conversion system	Energy storage system	Characteristics	Efficiency (η)	Reference No.
Dye-sensitized solar cell	Redox flow battery	The active energy storage materials were shared between dye-sensitized solar cells and redox flow batteries. A real energy storage capacity of 180 mWh cm ⁻² was obtained by choosing iodide/polysulfide as the pair of active materials along with permeable porous electrodes. The initial discharge capacity of the battery was 0.0153 mAh mL ⁻¹ in the voltage range of 0.2–0.76 V. A discharge capacity of 0.0151 mAh mL ⁻¹ was retained after 10 cycles.	$\eta_{conversion} = 1.7\%$ $\eta_{storage} = 100\%$ $\eta = N/A$	2
Dye-sensitized solar cell	Supercapacitor or	Anodic titanium oxide nanotube arrays were used as electrode materials for both dye-sensitized solar cells and electrochemical supercapacitors. Dye-sensitized solar cells with anodic titanium oxide nanotube arrays exhibited a short-circuit current density of 9.03 mA/cm ² , an open-circuit voltage of 0.63 V, and a fill factor of 57.55%. The ATO-based electrochemical supercapacitors could be photo-charged to approximately 0.6 V and the energy density was 6.662x10 ⁻⁸ Wh cm ⁻² .	$\eta_{conversion} = 3.17\%$ $\eta_{storage} = 51.6\%$ $\eta = 1.64\%$	3
		Solid electrolyte was inserted between two carbon nanotube films, and then a dye-coated TiO ₂ electrode was integrated onto the carbon nanotube films as an energy conversion device. Polyaniline was incorporated into the carbon nanotube films to improve the electrical conductivity of the electrode. The integrated device was photo-charged to 0.73 V in 183 s and then maintained at this value. The galvanostatic discharge time was 137 s under a constant current density of 1.4 mA cm ⁻² . The specific capacitance was 83 F g ⁻¹ , and the energy storage efficiency was calculated to be 34% with an energy conversion and storage efficiency of 0.79%.	$\eta_{conversion} = 6.1\%$ $\eta_{storage} = 84\%$ $\eta = 5.12\%$	4
		Wire-shaped energy conversion and storage devices were fabricated with Ti wire as the shared electrode. The dye-sensitized solar cells and supercapacitor were integrated in series. The Ti wire surface was modified with aligned titania nanotubes and then twisted with aligned carbon nanotube fibres. A low fill factor of 38% was obtained due to poor contact between the Ti wire and carbon nanotubes. The energy density of the CNT-based energy storage part was calculated to be 1.5x10 ⁻⁷ Wh cm ⁻² when the device was photo-charged to 0.6 V.	$\eta_{conversion} = 2.2\%$ $\eta_{storage} = N/A\%$ $\eta = 1.5\%$	5
		Flexible wire-shaped energy devices were fabricated using dye-sensitized solar cells and a supercapacitor, in which a stainless steel wire coated with PANi via anodic deposition was used as the electrode. The gel-based electrolyte solar cell showed a low efficiency of 1.21%, which was far lower than the efficiency of the liquid-based electrolyte cell. The device delivered a maximum areal capacitance of 41 mF cm ⁻² .	$\eta_{conversion} = 5.41\%$ $\eta_{storage} = 46\%$ $\eta = 2.12\%$	6

		<p>Solid-state, wire-shaped energy devices were demonstrated by coaxially integrating dye-sensitized solar cells and electrochemical capacitor into the Ti wire. Because a melted solid electrolyte was used, the photovoltaic efficiency of the solar cell was lower than those of conventional liquid electrolytes. The maximum energy conversion and storage efficiency was 2.73%, whereas the energy storage efficiency was 75.7% with specific capacitances up to 3.32 mF cm⁻².</p>	$\eta_{conversion} = 2.73\%$ $\eta_{storage} = 75.7\%$ $\eta = 1.83\%$	7
		<p>A silicon wafer was processed into a multifunctional platform where one side was adapted to enable triiodide reduction in a dye-sensitized solar cell and the other side provided on-board charge storage as an electrochemical supercapacitor. The energy density of the silicon-based electrochemical supercapacitor was calculated to be 0.17 μWh cm⁻² when it was photo-charged to 0.64 V.</p>	$\eta_{conversion} = 4.8\%$ $\eta_{storage} = 80\%$ $\eta = 2.10\%$	8
		<p>Counter electrodes of dye-sensitized solar cells were modified by poly (vinylidene fluoride)/ZnO nanowire arrays and used as active materials to fabricate a photo-rechargeable capacitor due to the high dielectric constant of poly (vinylidene fluoride) and high surface area of nanomaterials. The efficiency of the dye-sensitized solar cells with a modified counter electrode was lower than that of the non-modified solar cell (7.32%). The energy storage system utilized the electric polarization of PVdF. The photo-charged charge density was 2.14 C g⁻¹ because of PVdF, whereas the maximum energy conversion and storage efficiency were 3.70%.</p>	$\eta_{conversion} = 4.36\%$ $\eta_{storage} = \text{N/A}$ $\eta = 3.7\%$	9
Quantum dot-sensitized solar cell	Supercapacitor or	<p>Quantum dot-sensitized solar cells were integrated with a supercapacitor by sharing the carbon-coated mesh electrode. For solar cells, the Cu₂S layer on the mesh electrode was used as the active material. The mesh electrode solar cell exhibited a much lower efficiency than the double-side counter electrode cell (1.83%). The carbon-coated mesh fibre-based supercapacitor was photo-charged and galvanostatically discharged in a low voltage range of < 0.24 V.</p>	$\eta_{conversion} = 0.15\%$ $\eta_{storage} = \text{N/A}$ $\eta = \text{N/A}$	10
Dye-sensitized solar cell	Lithium ion battery	<p>A series-connected dye-sensitized solar cell and a lithium ion battery were integrated on the same Ti foil with double-sided TiO₂ nanotube arrays. For high voltage output, two solar cells were stacked directly, and they exhibited an open-circuit voltage of 3.39 V and a short-circuit current density of 1.01 mA/cm². The lithium ion battery with the conventional design, which utilized LiCoO₂ as the cathode and TiO₂ nanowires directly grown on the Ti foil as the anode, can be photo-charged to 3 V in about 8 min. Its discharge capacity was 38.89 μAh under a constant current density of 100 μA.</p>	$\eta_{conversion} = \text{N/A}$ $\eta_{storage} = 41\%$ $\eta = 0.82\%$	11
	Lithium oxygen battery	<p>A triiodide/iodide redox shuttle was used to couple a built-in dye-sensitized titanium dioxide photoelectrode with an oxygen electrode for photo-charging a lithium–oxygen battery. Due to the contribution of the photo-voltage, the charging overpotential was reduced from ~3.80 to ~3.40</p>	$\eta_{conversion} = \text{N/A}$ $\eta_{storage} = \text{N/A}$ $\eta = \text{N/A}$	12

		V.		
	Lithium sulfur battery	A photo-rechargeable lithium–sulfur battery was demonstrated by oxidizing S ²⁻ ions to polysulfide ions in an aqueous solution with a Pt-modified CdS photocatalyst. The battery delivered ~792 mAh g ⁻¹ after 2 h irradiation using a 500 W Xe-lamp; however, its long-term cycling stability was not demonstrated under irradiation.	$\eta_{conversion} = \text{N/A}$ $\eta_{storage} = \text{N/A}$ $\eta = \text{N/A}$	13
Perovskite solar cell	Supercapacitor or	A supercapacitor was fabricated on a printed perovskite solar cell using a shared PEDOT-carbon electrode. After exposure to air for 5 days, the short-circuit current density was decreased from 18.62 to 15.80 mA/cm ² as a result of the slight degradation of MAPbI ₃ by the residual water in isopropanol. The supercapacitor with the anion-doped PEDOT-coated carbon as electrodes can be photo-charged to ~0.6 V, and the energy density was calculated to be 7.83x10 ⁻⁷ Wh cm ⁻² .	$\eta_{conversion} = 6.37\%$ $\eta_{storage} = 73.77\%$ $\eta = 4.70\%$	14
Organic solar cell	Supercapacitor or	Solid-state supercapacitors were constructed by inserting a polymer-based electrolyte between single-wall carbon nanotube films, and then, the supercapacitors were integrated in parallel with multilayer organic solar cells. Two organic solar cells with an open-circuit voltage of 0.6 V were connected in series to increase the voltage output. The device can be photo-charged to ~0.6 V, and the discharge capacity of the device was able to retain up to ~47% of its initial value (17.5 g ⁻¹). In addition, the device exhibited a relatively short self-discharge life span (~60 min). The poor capacity retention and short self-discharge life span of the device may be attributed to the degraded energy conversion capability of the OPV under ambient conditions.	$\eta_{conversion} = 3.39\%$ $\eta_{storage} = \text{N/A}$ $\eta = \text{N/A}$	15
		Wire-shaped energy devices were demonstrated by integrating P3HT/PCBM and PEDOT/PSS layers as a solar cell and carbon nanotubes with PVA/H ₃ PO ₄ electrolyte as a supercapacitor. A surface-modified Ti wire was shared by the solar cell and supercapacitor. The supercapacitor delivered 1.61x10 ⁻⁷ Wh cm ⁻² under a constant current of 0.1 μA when photo-charged to ~0.4 V.	$\eta_{conversion} = 1.01\%$ $\eta_{storage} = 65.6\%$ $\eta = 0.82\%$	16

Supplementary Table S3. Photovoltaic parameters of the compact c-Si PV module in the SiPV-LIB device under various light intensity conditions.

Light intensity (mW cm ⁻²)	V_{oc} (V)	I_{sc} (mA cm ⁻²)	Cell area (cm ²)	J_{sc} (mA cm ⁻²)	FF (%)	Max power (mW)	PCE (%)
8	12.0±0.07	1.0±0.05	9	0.1±0.01	39.8±0.62	4.6±0.09	6.4±0.20
40	13.6±0.24	5.1±0.36	9	0.6±0.08	73.9±0.18	51.2±2.74	14.2±0.17
100	14.15±0.10	13.4±0.11	9	1.5±0.01	75.2±0.50	142.6±6.38	15.8±0.62

References

1. M. Bashahu and P. Nkundabakura, *Sol. Energy*, 2007, **81**, 856–863.
2. M. A. Mahmoudzadeh, A. R. Usgaocar, J. Giorgio, D. L. Officer, G. G. Wallace and J. D. W. Madden, *J. Mater. Chem. A*, 2016, **4**, 3446–3452.
3. J. Xu, H. Wu, L. Lu, S.-F. Leung, D. Chen, X. Chen, Z. Fan, G. Shen and D. Li, *Adv. Func. Mater.*, 2014, **24**, 1840–1846.
4. Z. Yang, L. Li, Y. Luo, R. He, L. Qiu, H. Lin and H. Peng, *J. Mater. Chem. A*, 2013, **1**, 954–958.
5. T. Chen, L. Qiu, Z. Yang, Z. Cai, J. Ren, H. P. Li, H. Lin, X. M. Sun and H. S. Peng, *Angew. Chem. Int. Ed.*, 2012, **51**, 11977–11980.
6. Y. Fu, H. Wu, S. Ye, X. Cai, X. Yu, S. Hou, H. Kafafy and D. Zou, *Energy Environ. Sci.*, 2013, **6**, 805–812.
7. X. Chen, H. Sun, Z. Yang, G. Guan, Z. Zhang, L. Qiu and H. Peng, *J. Mater. Chem. A*, 2014, **2**, 1897–1902.
8. X. Zhang, X. Huang, C. Li and H. Jiang, *Adv. Mater.*, 2013, **25**, 4093–4096.
9. A. P. Cohn, W. R. Erwin, K. Share, L. Oakes, A. S. Westover, R. E. Carter, R. Bardhan and C. L. Pint, *Nano Lett.*, 2015, **15**, 2727–2731.
10. C. Shi, H. Dong, R. Zhu, H. Li, Y. Sun, D. Xu, Q. Zhao and D. Yu, *Nano Energy*, 2015, **13**, 670–678.
11. W. Guo, X. Xue, S. Wang, C. Lin and Z. L. Wang, *Nano Lett.*, 2012, **12**, 2520–2523.
12. M. Yu, X. Ren, L. Ma and Y. Wu, *Nat. Commun.*, 2014, **5**, 5111.
13. N. Li, Y. Wang, D. Tang and H. Zhou, *Angew. Chem. Int. Ed.*, 2015, **54**, 9271–9274.
14. J. Xu, Z. Ku, Y. Zhang, D. Chao and H. J. Fan, *Advanced Materials Technologies*, 2016, 1600074.
15. G. Wee, T. Salim, Y. M. Lam, S. G. Mhaisalkar and M. Srinivasan, *Energy Environ. Sci.*, 2011, **4**, 413–416.
16. Z. Zhang, X. Chen, P. Chen, G. Guan, L. Qiu, H. Lin, Z. Yang, W. Bai, Y. Luo and H. Peng, *Adv. Mater.*, 2014, **26**, 466–470.